



THE UNIVERSITY *of* EDINBURGH

Edinburgh Research Explorer

The Physical Characteristics of a CO₂ Seeping Fault: the implications of fracture permeability for carbon capture and storage integrity

Citation for published version:

Bond, C, Kremer, Y, Johnson, G, Hicks, N, Lister, R, Jones, D, Haszeldine, R, Saunders, I, Gilfillan, S, Shipton, Z & Pearce, JM 2017, 'The Physical Characteristics of a CO₂ Seeping Fault: the implications of fracture permeability for carbon capture and storage integrity' *International Journal of Greenhouse Gas Control*, vol 61, pp. 49–60. DOI: 10.1016/j.ijggc.2017.01.015

Digital Object Identifier (DOI):

[10.1016/j.ijggc.2017.01.015](https://doi.org/10.1016/j.ijggc.2017.01.015)

Link:

[Link to publication record in Edinburgh Research Explorer](#)

Document Version:

Peer reviewed version

Published In:

International Journal of Greenhouse Gas Control

Publisher Rights Statement:

© 2017 Published by Elsevier Ltd.

General rights

Copyright for the publications made accessible via the Edinburgh Research Explorer is retained by the author(s) and / or other copyright owners and it is a condition of accessing these publications that users recognise and abide by the legal requirements associated with these rights.

Take down policy

The University of Edinburgh has made every reasonable effort to ensure that Edinburgh Research Explorer content complies with UK legislation. If you believe that the public display of this file breaches copyright please contact openaccess@ed.ac.uk providing details, and we will remove access to the work immediately and investigate your claim.



1 **The Physical Characteristics of a CO₂ Seeping Fault: the implications of fracture**
2 **permeability for carbon capture and storage integrity**

3
4 Clare E. Bond^{1*}
5 Yannick Kremer²
6 Gareth Johnson³
7 Nigel Hicks⁴
8 Robert Lister⁵
9 Dave G. Jones⁵
10 Stuart Haszeldine³
11 Ian Saunders⁶
12 Stuart Gilfillan³
13 Zoe K. Shipton²
14 Jonathan Pearce⁵

15
16 ¹Department of Geology and Petroleum Geology, University of Aberdeen, Meston Building,
17 Kings College, Aberdeen, AB24 3UE, UK (clare.bond@abdn.ac.uk)

18 ²Department of Civil and Environmental Engineering, University of Strathclyde, James Weir
19 Building, Glasgow, G1 1XJ (yannick.kremer@strath.ac.uk; zoe.shipton@strath.ac.uk)

20 ³School of Geosciences, University of Edinburgh, Grant Institute, Kings Buildings, James
21 Hutton Road, Edinburgh, EH9 3FE (g.johnson@ed.ac.uk; stuart.gilfillan@ed.ac.uk;
22 stuart.haszeldine@ed.ac.uk)

23 ⁴Council for Geoscience, 139 Jabu Ndlovu Street, Pietermaritzburg, KwaZulu-Natal, South
24 Africa 3200 (nhicks@geoscience.org.za)

25 ⁵British Geological Survey, Environmental Science Centre, Nicker Hill, Keyworth, Nottingham
26 NG12 5GG (trl@bgs.ac.uk; dgj@bgs.ac.uk; jmpe@bgs.ac.uk)

27 ⁶Council for Geoscience, 280 Pretoria St, Silverton, Pretoria, 0184 (ians@geoscience.org.za)

28 *Corresponding Author clare.bond@abdn.ac.uk

29
30
31
32 **Highlights**

- 33
34
 - CO₂ migration is spatially associated with the Bongwana fault fracture corridor.
 - Cap rock permeability suggests that without fractures it would act as a flow barrier.
 - Elevated CO₂ concentration and flux are measured across the fracture corridor.
 - Fracture intensity and orientation variability creates permeability heterogeneity.
 - Seismically unresolvable fracture networks may impact CO₂ storage capability.
- 35
36
37
38
39
40
41

42 **Abstract**

43 To ensure the effective long-term storage of CO₂ in potential geological storage sites,
44 evaluation of leakage pathways to the surface should be undertaken. Here we use a series
45 of natural CO₂ seeps along a fault in South Africa to assess the controls on CO₂ leakage to
46 the surface. Geological mapping and detailed photogrammetry reveals extensive fracturing
47 along the mapped fault trace. Measurements of gas flux and CO₂ concentration, across the
48 fracture corridor, give maximum soil gas measurements of 27% CO₂ concentration, and a
49 flux of 191 g m⁻² d⁻¹. These measurements along with observations of gas bubbles in streams
50 and travertine cones attest to CO₂ migration to the surface. Permeability measurements on
51 the host rock units show that the tillite should act as an impermeable seal to upward CO₂
52 migration. The combined permeability and fracture mapping data indicate that fracture
53 permeability creates the likely pathway for CO₂ migration through the low permeability
54 tillite to the surface. Heterogeneity in fracture connectivity and intensity at a range of scales
55 will create local higher permeability pathways along the fracture corridor, although these
56 may seal with time due to fluid-rock interaction. The results have implications for the
57 assessment and choice of geological CO₂ storage sites, particularly in the assessment of sub-
58 seismic fracture networks.

59

60 **Keywords**

61 Fracture permeability, CO₂ storage, leakage, natural analogue

62

1. Introduction

Climate change is generally recognized as a global 21st century challenge (Bernstein et al., IPCC, 2007). Anthropogenic greenhouse gas emissions, primarily CO₂, are extremely likely to have been the dominant driver of such change. CO₂ from fossil fuel combustion and industrial processes contributed 78% of the increase in GHG emissions between 1970 and 2010 (Field et al., IPCC, 2014). Carbon capture and storage (CCS) has been proposed to mitigate CO₂ emissions (Metz et al., IPCC, 2005). CCS is recognized as a bridging technology in energy production (e.g. Praetorius, and Schumacher, 2009), to mitigate the impact of CO₂ emissions, while renewable energy sources are developed. In order to expedite the deployment of CCS research is being undertaken to understand the reactivity and flow pathways of CO₂ in the subsurface (e.g Xu et al., 2003; Audigane et al., 2007) and to develop methods to measure, model and verify (MMV) geological CO₂ storage (Newell et al., 2008; Ringrose et al., 2013). Understanding the role of faults and fractures as fast fluid pathways, through overburden strata, to the surface is critical to ensure storage verification for engineered CCS sites.

Fracture controlled flow of CO₂ has been implicated in compromising the integrity of pilot CCS sites. For example, injection of CO₂ was halted at the In Salah CO₂ CCS pilot site due to the role of fractures in creating a conductive network through which CO₂ could migrate (e.g. Bond et al., 2013; Rinaldi and Rutqvist, 2013). To better understand the role of faults and associated fracture damage on controlling CO₂ flow pathways and flux rates, natural CO₂ seeps have been studied (e.g. Roberts et al., 2015). Examples of natural CO₂ seeps along faults include: the Paradox Basin Utah (e.g. Shipton et al., 2006); and the Apennines of Italy (e.g. Miller et al., 2004; Roberts et al., 2015). Here we describe the structural characteristics of the CO₂ seeping Bongwana Fault in KwaZulu-Natal, South Africa; to better constrain fracture and fault controlled CO₂ flow to the surface.

The Bongwana Fault is one of only two known examples of naturally seeping CO₂ in South Africa. The fault was identified during geological mapping between 1911-1916 by du Toit (1920), with CO₂ de-gassing along the fault first described by Young (1924). We present the first modern structural study of the physical characteristics of the fault, in terms of field exposure or a physical analysis of rock properties. We present new structural data from key locations where active CO₂ seeps occur along the fault as identified by Gevers (1941) and du Toit (1920). A hypothetical model of fracture-controlled permeability is proposed and refined by the field data. The results are discussed in the context of site selection and characterization at CCS sites where faults and fractures might play a role in permitting escape of CO₂ from a reservoir.

2. Geological Setting

The Ntlakwe-Bongwan Fault was identified during the mapping of Pondoland (Eastern Cape Province) and parts of the Alfred and Lower Umzimkulu Counties (KwaZulu-Natal) by du Toit (1920). The fault truncates sedimentary and igneous units of the Karoo Supergroup, as well as units of the Msikaba Formation in the south (Johnson et al., 2006). Within the study area, tillites and minor shales of the Dwyka Group, Karoo Supergroup, form the dominant surface lithologies. The tillite in southern KwaZulu-Natal has a thickness of ~450m (Thomas et al., 1990) and unconformably overlies coarse-grained sandstones and conglomerates of

110 the Msikaba Formation. The Msikaba Formation represents the assumed CO₂ reservoir,
111 occurring as a 450m thick package in the Port Shepstone area which thickens southwards to
112 900m north of Port St Johns (Kingsley and Marshall, 2009).

113

114 The fault crops out on the surface over a trace length of 80 km (De Decker, 1981) with its
115 northern extension known as the Bongwan, or Bongwana Fault (De Decker, 1981; Harris et
116 al., 1997). The fault is related to Gondwana break-up which began at 180 Ma and continues
117 today (Watkeys and Sokoutis, 1998). The zone of faulting in southern KwaZulu-Natal is
118 about 70 km wide and defined by arcuate fault traces that change southwards from ENE-
119 WSW to a north-south strike (Watkeys and Sokoutis, 1998). These fault systems correlate
120 with the early stage, arcuate, Type I fault systems defined by Von Veh and Andersen (1990)
121 in northern KwaZulu-Natal. Passive continental margin conditions have predominated since
122 the late Jurassic (Maud, 1961; Dingle and Scrutton, 1974) with offshore faulting evident until
123 the Cenomanian (Singh and McLachlan, 2003). The southeastern portion of southern Africa
124 was subject to intense periods of epiorogenic uplift resulting in a marked onshore hiatus
125 from the late Eocene to middle Miocene times (King, 1972; Frankel, 1972; Dingle and
126 Scrutton; 1974; Grab and Knight, 2015), as well as in the Pliocene, where ~900m of uplift is
127 postulated by Partridge and Maud (2000). To-date no faulting related to these uplift
128 episodes has been recorded onshore, likely due to the erosional conditions that have
129 prevailed since the early Cretaceous. Present day seismic activity is minimal, although a
130 survey of micro-tremors using a single-station location method undertaken as a separate
131 part of this study indicates a possible micro-earthquake of M~0.5 in 2007, the epicentre of
132 which locates on the northern section of the Bongwana Fault near the abandoned gas works
133 on Lot 7 (Site A – this study; see Figure 1).

134

135 Due to the homogeneous nature and thickness of the Dwyka Group tillites, fault
136 displacement within the study area is hard to quantify. There are no mappable stratigraphic
137 offsets in the study area (Figure 1). However, to the south along the Londobezi River a large
138 graben is developed between two splays of the fault in which Ecca Group and Karoo Dolerite
139 Suite rocks are preserved. Gevers (1941) suggests vertical offset in this region of 579m
140 (1900 feet) with all units within the graben truncated by the fault system. These truncations
141 allow for a maximum age definition for the faulting of ~179 Ma, based upon ⁴⁰Ar/³⁹Ar dating
142 by Duncan et al., (1997) for the Karoo Dolerite Suite.

143

144 Watkeys and Sokoutis (1998) indicate that, due to intense subtropical weathering, the
145 faulting pattern in southern KwaZulu-Natal is difficult to interpret. In areas of brecciation
146 and silicification, the faults have a positive relief, a considerable aid to the delineation of the
147 fault systems (Thomas, 1988). Gevers (1941) also describes the fault in many locations as a
148 silicified feature that stands “proud of the ground”, with a range in the fault (fracture zone)
149 width of between 0.3 m – 10 m wide. Gevers (1941) describes the fracture zones as being
150 lenticular in shape and cropping out intermittently. The fault zone is chemically altered and
151 marked by degradation of the tillite to a white, apparently pulverized, rock. The whitening
152 of the rock is from the extensive kaolinisation and leaching of the tillite by CO₂ rich water
153 (Gevers, 1941). According to Gevers (1941), within the Bongwana region, du Toit (1920)
154 mapped splay and minor faults on either side, and parallel or sub-parallel, to the main fault,
155 with splays extending for up to 1.6 km in length.

156

157 Young (1924) provided the first description of CO₂ degassing from Bongwana fault fissures.
158 In his recordings of the exposure on Farm Lot 7 (Site A – this study), Young (1924) described
159 CO₂ gas steadily bubbling to the surface in the Umzimkulwana River close to its west bank. It
160 was at this site that a CO₂ bottling plant was established around 1924 to capture the CO₂
161 exhalations for commercial use (Gevers, 1941). On the neighboring farm (Lot 10), Young
162 (1924) identified a two feet wide vertical zone of brecciated Dwyka Group tillite from which
163 CO₂ de-gassed. Significantly higher CO₂ flux was noted by Young (1924) along the contact of
164 brecciated Dwyka Group tillite with non-brecciated tillite described as being altered to soft
165 clay. Analyses of the two gas samples, collected by Young (1924), gave CO₂ compositions of
166 98.3 % and 97.6 %. Gevers (1941) provides the most extensive description of the field sites
167 seeping CO₂, including analysis of the gas. Further studies of the gas chemistry, including
168 stable isotope analyses have been completed by Harris et al. (1997), reporting the CO₂ to
169 have a $\delta^{13}\text{C}$ of -0.6 ‰ - +0.9 ‰ (PDB) and $\delta^{18}\text{O}$ 35.3-45.1 ‰ (SMOW). Gevers (1941) and
170 Harris et al. (1997) suggest the CO₂ is sourced from the reaction of acidic ground water with
171 carbonate rocks at depth. This hypothesis is plausible, as carbonate rocks of the Marble
172 Delta Formation are seen cropping out ~30 km east of Bongwana (Figure 1), along structural
173 basement strike, as a folded protolith enclave within Meso-proterozoic basement lithologies
174 (Otto, 1973). Conversely with Hartnady (1985) who suggests generation of CO₂ by a mantle
175 plume, with early carbonatite magma generation. Whatever the source, CO₂ has been
176 seeping from the fault for some time because a series of travertine cones with CO₂ springs,
177 some now dormant (Gevers, 1941; and observed in this study) attest to significant volumes
178 of CO₂ over, at least, hundreds of years. Two of the localities identified by Gevers (1941)
179 were visited, as well as a third mapped as a CO₂ exhalation by du Toit (1920). These
180 locations are shown in Figure 1.

181
182

183 3. Models for CO₂ flow to the surface

184 Significant work has been undertaken within the oil and gas sector to determine the
185 controls on the sealing capacity of faults (Yielding et al., 1997; Manzocchi et al., 1999;
186 Bretan et al., 2003) and overburden caprocks (Grunau, 1987; Watts, 1987) to hydrocarbon
187 fluids. This work is being used to inform predictions of the storage capacity and viability of
188 potential CCS sites (Li et al., 2005; Li et al., 2006; Shukla et al., 2010), although it is
189 recognized that faults and fractures may respond differently to CO₂, especially when
190 pressurized CO₂ is injected (Rutquist, 2012; Verdon et al., 2015). Faults are known to act as
191 both barriers and conduits to fluid flow (Sibson, 1995; Caine et al., 1996; Bense and Person,
192 2006), with the permeability characteristics of the fault plane and associated damage zone
193 combining to determine a fault's overall permeability (Caine et al., 1996; Foxford et al. 1998;
194 Aydin and Eyal, 2002). The geometry and heterogeneity of the whole fault zone, down to
195 the micro-scale, determine a fault's permeability. Work on understanding and predicting
196 fault (and off-fault) damage and its implications for permeability have mainly focused on
197 normal faults within siliciclastic reservoir sequences (Caine et al., 1996; Hesthammer et al.,
198 2000; Shipton and Cowie, 2003; Fossen et al., 2007; Farrell et al., 2014). Understanding of
199 fault zone characteristics in other lithologies is less well developed, especially in relation to
200 capacity for fluid flow. Studies on fault damage and implications for permeability in other
201 lithologies include carbonates Agosta and Kirschner, (2003), Haines et al. (2016); basalts
202 (Walker et al., 2013); and granitic gneiss (Lawther et al., 2016). A fault zone's potential to

203 act as a conduit for fluid is dependent on a number of factors that are not easily predicted
204 (Fossen et al., 2007; Faulkner et al., 2010; Farrell et al., 2014).

205

206 A series of hypothetical models (Figure 2) show a range of potential fault zone
207 permeabilities that may allow CO₂ flow to the surface at Bongwana. The models are based
208 on understanding of different fault-rock permeabilities, originally proposed by Caine et al.
209 (1996); and developed by others. Faulkner et al. (2010) give a summary. Here we consider
210 these models by collection of field data and observations along the Bongwana Fault,
211 combined with laboratory analysis to propose a site-specific model of CO₂ flow to the
212 surface for Bongwana for future testing.

213

214 **4. Methodology**

215 A range of methodologies were employed to capture the structural characteristics of the
216 Bongwana fault zone in an attempt to determine the potential role of the fault and
217 associated fractures as pathways for CO₂ to the surface. Initial regional scale analysis was
218 completed prior to field data collection using GoogleEarth™ and Aster imagery in
219 combination with published geological maps (Gever, 1941; Thomas, 1988). In the field,
220 these data were combined with GPS locations and structural measurements. High-
221 resolution digital photography of fault zone outcrops were utilized for photogrammetry to
222 create 3D virtual outcrop models. Desk-top digital analysis of the virtual outcrop models
223 augment the in-field structural measurements. Outcrop scale maps of fault architecture
224 were completed along with structural measurements and further detailed photography.
225 Structural characterisation is augmented by gas (CO₂) flux and concentration measurements
226 made at a single site and porosity and permeability measurements of the assumed reservoir
227 (Msikaba Formation sandstones) and seal (Dwyka Group tillites) rocks. Each method
228 employed is described in turn.

229

230 **4.1 Structural Data**

231 The app Fieldmove was used on an iPad Air 2 for collection of all structural data. Pre-loaded
232 geo-tiffs of existing field maps and OpenStreet Map (mapbox.com) imagery were used in the
233 field to aid in field site identification. In-field tracking was enhanced by Bluetooth
234 connection of the iPad to a Garmin GLO for GPS and GLONASS location sensing. In-app
235 functionality allows the user to define locations, take notes as in a field notebook, and take
236 photos through access to the iPad's digital camera. Further, the app utilises the
237 magnetometer, gyroscope and accelerometer within the iPad's hardware for use as a
238 compass clinometer. Measurements of fracture orientation and dip were made and
239 recorded directly on the iPad.

240

241 **4.2 Virtual Outcrop Models**

242 A Nikon D3200 SLR was used with a fixed lens (35mm) to collect digital photographs of
243 outcrops for photogrammetry. The method requires multiple photographs to be taken
244 orthogonal to the outcrop surface, with an approximate 60 % over-lap. The photographs are
245 georeferenced and a scale and orientation is used in each photo-set to allow for later scaling
246 and geo-referencing of the virtual outcrop models. Each evening the photographs were
247 downloaded and processed in Photoscan-pro software to create a 3D virtual outcrop model.
248 The technique and its use in geology is described by various authors (e.g. Roncella et al.,
249 2005; Bemis et al., 2014; Johnson et al., 2014; Salvini et al., 2015). Creating virtual outcrop

250 models during the fieldwork allows for checks to be made of the photogrammetric model to
251 see if the photographs have the required overlap and coverage, so that further photos may
252 be acquired if needed to create a full virtual outcrop model.

253

254 Oriented ortho-rectified photographs (orthophotos) were created from the virtual outcrop
255 models; these were imported into Move software, scaled and geo-referenced, where digital
256 interpretation of the fracture sets was undertaken. The pixel size of the imagery was kept
257 constant at 300 dpi. The software is used to determine fracture attributes, such as
258 orientation and length; as well as to determine if multiple fracture sets are present. The
259 digitised fracture datasets were input into a MATLAB script to determine fracture intensity
260 for each virtual outcrop using the circular scan-line method of Mauldon et al. (2001).

261

262 **4.3 Gas Flux and Composition Sampling**

263 Soil gas measurements were made using probes consisting of an 8 mm diameter (4 mm
264 internal diameter) stainless-steel tube onto which two solid steel cylinders were welded to
265 act as pounding surfaces when installing and removing the probes with a co-axial hammer.
266 Prior to insertion, a sacrificial tip was fitted to the bottom of the probe to prevent blockage.
267 The probes were inserted to a depth of 85-90 cm. In situ soil gas measurements of CO₂, H₂S,
268 CH₄, and O₂ concentrations were made using a Geotechnical Instruments GA2000 portable
269 gas analyser. CO₂ flux measurements were taken using a West Systems portable flux meter
270 with a LICOR LI-820 IR detector connected via Bluetooth to a Trimble Juno palm-top
271 computer (PDA) with built-in GPS. Measurements took 1–3 min depending on the soil flux
272 rate. Flux was measured before soil gas to minimise disturbance of the flux. The instruments
273 were calibrated before and after the fieldwork using certified calibration gases.

274

275 **4.4 Porosity and Permeability Analysis**

276 Porosity and permeability analyses were made on samples of Msikaba Formation sandstone
277 (3 orthogonal cores) and Dwyka Group tillite, from outside the obvious fault/fractured area
278 (2 cores – at right angles). Porosity measurements were made on core samples using helium
279 (He) gas, on an Edinburgh Petroleum Ltd, Mk. 2 Helium gas porosimeter. Permeability
280 measurements were made on the core samples using a Jones permeater with nitrogen (N₂)
281 gas. A Hassler sleeve was used to pressurize the sample to 400 psi (2.76 MPa), and five
282 repeat measurements at different fluid pressures on the high pressure gauge were
283 measured. The results were corrected using a Klinkenburgh correction and the mean value
284 used.

285

286 **5. Results and Analysis**

287

288 Within the study area the fault is expressed in a series of outcrops that are relatively sparse
289 with respect to the fault length and which vary in character from highly fractured zones to
290 apparently 'pulverised' rock. Nowhere is the full width of the fault obviously exposed. Small
291 sections of fractured Dwyka Group tillite are observed. The fault zone surface expression is
292 defined by distributed fractured rock outcrop, defining a fracture corridor, rather than a
293 discrete single fault surface, or fault slip plane and damage zone. Three localities of CO₂
294 degassing along the fault trace informed the study (Figure 1).

295

296 Site A, occurs on Farm Lot 7 alongside the Umzimkulwana River east of Bongwana rail siding.
297 Here CO₂ is observed effervescing in the Umzimkulwana River where the road bridge
298 crosses the river; on the western bank of the river pools of water in river bank sand also
299 show CO₂ bubbles. The outcrop at Site A is approximately 2.5 m x 1.5 m, sited next to the
300 river and consists of fractured Dwyka Group tillite. The exhalations at this site have a high
301 flux rate with Gevers (1941) indicating that exhalations identified on the neighbouring farm,
302 Lot 10, measured 30 ft³ minute⁻¹ (0.014 m³s⁻¹) from a 5 inch (0.127 m) diameter pipe in
303 1924.

304
305 Site B (Figure 1), occurs 9 km south of Site A on the Manzimhlanga River, near Mjaja; here
306 several outcrops of faulted and fractured Dwyka Group tillite crop out. CO₂ de-gassing is
307 observed as bubbles in the nearby river, but the volume is minimal in comparison to Site A.
308 Three distinct outcrops are described at Site B, which are characterized both by leaching and
309 whitening of the rock, but with areas of iron staining and some silicification.

310
311 Site C (Figure 1) is the southernmost of the known CO₂ emissions along the Bongwana Fault
312 occurring on the northern and southern banks of the Umtamvuna River where well
313 developed travertine cones and CO₂ springs are identified. Four travertine cones are
314 developed atop large travertine mounds ~50-100m in diameter. Two cones occur on the
315 northern bank and are by far the largest (~15m diameter). These cones are only partially
316 active with minor CO₂ gas and water seeps identified. On the southern bank, two smaller
317 cones are identified, both of which are active. Both issue CO₂ gas and water, with the larger
318 "Cone Spring" represented by a steep-sided cone ~1 m in diameter and 80 cm high. The
319 other spring occurs ~5 m east, as a flat cone termed the "Mound Spring". As well as basic
320 mapping of the travertine cones, structural measurements were made at two key localities
321 in the vicinity of the cones where fractured and brecciated outcrops were observed that
322 have not previously been described.

323
324

325 **5.1 Regional Trend and Structural Data**

326 The outcrops visited are linearly aligned, approximately North-South over a horizontal
327 distance of 15 km. The outcrops fall on the line of the Bongwana fault mapped by du Toit
328 (1920) and published by Gevers (1941) (Figure 3).

329
330 Fracture orientations were measured at all three localities. Primary fractures identified in
331 the field have N-S trends (Figure 3a – rose diagrams). Poles to fractures at Sites A, B and C
332 have kappa distributions of 1.13, 2.58 and 2.5 respectively (where smaller kappa indicates a
333 tighter clustering of fracture orientations). The fractures are sub-vertical with a mean dip
334 between 82°-89° at the three sites. Fractures dip in both directions around a mean fracture
335 strike for Site A of 169° and at Site C 006°. The fractures measured at Site B appear more
336 dispersed in nature (Figure 3a) with a mean fracture strike orientation approximately NE-SW
337 (a mean dip of 82° and a strike direction of 029°), but with significant dispersion within the
338 NE and SW stereonet segments (Figure 3a).

339
340 At Sites B and C multiple sub-sites form the dataset (Figure 3c and d) between 20 and
341 several 100 m apart. Stereonet plots from individual outcrop sub-sites show more
342 consistency in fracture strike orientation, so the dispersion in fracture orientation is created

343 from the amalgamation of the fracture data collected at the multiple sub-sites. Outcrop site
344 *Bi* shows a fracture distribution similar to Site A with a predominant primary fracture set
345 trend of approximately N-S, with a NW-SE oriented secondary fracture set. Sites *Bii*, *iii*, *iv* all
346 show fractures in a NE-SW direction. At site *Bii* a NE-SW fracture strike is most prevalent.
347 The rock here appears grey-white in colour and has the consistency of white flour when
348 hammered. Sites *Bii* and *Biii* c. 20 m apart, are linked by almost continuous outcrop, in
349 which the along-strike change in fracture trend can be observed. The mean fracture dip at
350 site *Bii* is 82°, with a mean strike of 055°; at site *Biii* the mean dip is 82° with a mean strike of
351 026°. At site *Biii* the fractures dip consistently to the east. The rock character also changes,
352 as you move away from the apparently pulverized rock at *Bii* into the coherent rock at *Biii*
353 where primary and secondary fracture sets can be identified. Often the secondary fractures
354 form with horsetail geometries, splaying from primary fractures or filling the rock space
355 between approximately N-S oriented primary fractures. These geometries are also identified
356 in analysis of the virtual outcrop models and fault architecture mapping. The change in
357 fracture orientation at site B corresponds to a bend in the fault line on the surface,
358 according to the mapping of du Toit and Gevers (1941). This bend changes the fault
359 orientation from approximately N-S 006° at Site C to an approximate NE-SW 029° at Site B,
360 (Figure 3b).

361

362 At two sites slickensides could be measured on fracture/fault surfaces. At Site *Cii* a small
363 fracture surface oriented with a strike of 013 and a dip of 82° had three measurable
364 slickensides. The mean slickenside trend is 337 with a plunge of 77°. The slickensides are
365 approximately dip-slip (vertical) (figure 3b). At Site *Biv* a larger fracture/fault surface is
366 exposed with numerous slickensides, 14 slickenside lineation measurements were made on
367 the surface. In figure 3b a mean fracture plane surface is plotted (great circle) with a strike
368 of 031 and a mean dip of 82°, the slickensides are sub-parallel with a mean slickenside trend
369 is 050 with a plunge of 72°. The slickensides at Site *Biv* are slightly oblique to dip-slip, by c.
370 20° to the NE.

371

372 **5.2 Fault Architecture Mapping from Virtual Outcrop Models**

373 Virtual outcrop models were made at all three sites. Virtual outcrop models of five fractured
374 surfaces from the three sites have been digitally interpreted on orthorectified photographs.
375 Fracture orientations derived from the models (Figure 4a-e, stereonet), are consistent with
376 in-field measurements (Figure 3, stereonet), with a main fracture set trending c. N-S and
377 secondary sets either trending c. E-W, or as a conjugate set bisecting an E-W trend. Mapped
378 fractures at Site *Bi* and *Biii* (Figure 4b and 4c), show the horsetail geometries and fracture
379 splays.

380

381 Using a custom MATLAB script, we use the circular scanline method of Mauldon et al. (2001)
382 to create fracture density plots (number of fractures per m²) for each digitally interpreted
383 outcrop (Figure 4a-e). This approach defines a circular sampling window, from which the
384 number of fracture endpoints (m) within the circle and the number of fracture intersections
385 (n) with the circle are recorded. From these two statistics, the fracture density, intensity and
386 mean trace length can be calculated. The script uses a moving window approach to calculate
387 the statistics for a large number of circles at different locations, resulting in a map of
388 fracture intensity variation. The accuracy of this method depends on the number of
389 endpoints in the circle, and therefore on the size of the circle compared to typical fracture

390 spacing. Rohrbaugh et al. (2002) suggest that the scan-circle radius should exceed typical
391 block size. To accurately determine the minimum scan radius required for our fracture
392 maps, we calculate these statistics for different circle radii at several locations. Figure 5
393 shows a plot of the three properties, density, intensity and mean trace length, against circle
394 radius for site Ci. At this location, the statistics stabilise at a fracture radius of at least 8 cm.

395 The fracture density maps created can be used to visualise and examine the heterogeneity
396 of the fracture network. Calculated values are artificially low near the edges of the map, as
397 no fractures are mapped in poorly exposed areas. As such, representative values for the
398 fracture density at this location must be taken at least one radius distance (8 cm) away from
399 the edge of the rock outcrop. This results in typical fracture densities ranging from 1500 –
400 3000 fractures m⁻² at Site Ci. For this site fracture intensity ranges from 40 to 120 fractures
401 m⁻¹, and mean trace lengths range from 5 to 15 cm. At the nearby site Cii, 100 m away, the
402 fracture density is a maximum of 11 fractures m⁻² (Figure 4e). Fractures are mainly unfilled,
403 e.g. Sites A and C At these site where red-brown staining around the fractures (thin halos up
404 to 0.5cm) and coatings on fracture surfaces is interpreted as evidence for past fluid-flow. At
405 Site B fractures appear to be cemented, as part of the pervasive (in the vicinity to fractures)
406 chemical alteration of the rock.

407

408 **5.3 Gas Flux and composition measurements**

409 Gas flux and composition measurements were made at Site C along a transect perpendicular
410 to and crossing the trend of the main fault line. The locality chosen was on the Northern
411 bank of the Umtamvuna River between mapped active gas exhalations (Figure 6). The
412 results of the gas flux and composition measurements are shown in map view, with circles
413 scaled for flux (Figure 6a) and graphically (Figure 6b). Falling on the predicted fault line (zero
414 on the x-axis of the graph) the maximum percentage of CO₂ in the captured gas is 27 %, with
415 a flux of 191 g m⁻² d⁻¹. Away from the predicted fault line (50-80 m) the flux and CO₂
416 composition recorded diminish to 1 % or below, and 17-26 g m⁻² d⁻¹. A symmetrical pattern
417 is seen on either side of the fault with no observed difference in the footwall or hangingwall
418 of the structure. The results support the assertion that the fault and associated deformation
419 structures are controlling migration of CO₂ to the surface.

420

421 **5.4 Porosity and Permeability data**

422 Porosity and permeability measurements were made on three orthogonal cores of Msikaba
423 Formation sandstone collected in the Oribi gorge. The sandstone is quartz dominated and
424 shows a coarsening-upward sequence within beds. The sample, of a bed approximately 20
425 cm thick, contains quartz pebbles (2-10 mm) at its base fining up to <1 mm. The cores were
426 taken across bedding and in two orthogonal orientations parallel to bedding.
427 Samples of apparently undeformed and unaltered Dwyka Group tillite from Site Bii, less than
428 1 m from highly altered tillite in the 'fault zone', were also cored in two orthogonal
429 directions. The tillite has a fine-grained grey matrix with clasts in the samples up to 10 mm
430 in diameter, but generally clasts are 2-3 mm in size. Samples of fractured and altered tillite
431 disintegrated when cut or cored using water-cooled mechanisms, supporting the assertion
432 of alteration to clays, so were not suitable for core analysis.

433

434 The results of the analyses are shown in Table 1. The unaltered Dwyka Group tillite has a
435 high porosity (c. 20%), compared to the Msikaba Formation sandstone (c. 4-5%) but a lower
436 effective permeability 1×10^{-2} . Figure 7 shows the samples plotted on a porosity-
437 permeability plot alongside data from different types of sandstones from Lake (2007) -
438 Society of Petroleum Engineers (SPE) (Petrowiki, accessed 2016). The Msikaba Formation
439 sandstone falls within the range of consolidated sandstones (0.18 -0.27 mD), whilst the
440 tillite has a permeability at the lower end of consolidated sandstone and the top end of tight
441 sands (0.06 – 0.07 mD).

442

443 **6. Discussion**

444

445 The Bongwana Fault is unusual in its expression. Our observations of dip-slip slickensides on
446 steeply dipping fracture surfaces support those of Gevers (1941) who described dip-slip
447 slickensides on an almost vertical fault. However, no distinct fault surface is observed in the
448 field. The fault displacement-length characteristics at the lower end of those predicted by
449 global compilations (e.g. Walsh and Watterson, 1988; Schlische et al., 1996; Kim and
450 Sanderson, 2005). For an 80 km long normal fault, displacement in the order of 80 m-8 km
451 would be expected based on the range of published displacement length data, compared to
452 the 579 m estimated throw observed by Gevers (1941). These observations suggest that the
453 Bongwana Fault is a deep-seated basement fault, or series of amalgamated faults that may
454 have had an earlier strike-slip history. Given the lack of observed piercing points, the
455 amount of strike slip on the fault is not quantified.

456

457 Porosity and permeability measurements of selected rock samples attest to a potential CO₂
458 reservoir at depth and an effective cap rock seal. The Dwyka Group tillite (assumed cap-rock
459 seal) has a high porosity but low effective permeability (1×10^{-2} mD). Incontrast, the
460 permeability of the assumed CO₂ reservoir, the Msikaba Formation sandstone, is 1×10^{-1} mD,
461 within the range of known consolidated sandstones that form hydrocarbon reservoirs,
462 whereas the tillite has a permeability at the high-end of tight sands (Figure 7). Tight sand
463 reservoirs in a hydrocarbon setting are reliant on fracture permeability for effective
464 hydrocarbon flow. The fractures identified in the field associated with the Bongwana Fault
465 are therefore the likely conduit for CO₂ from the Msikaba Formation sandstone to the
466 surface.

467

468 The dominant fracture set parallels the fault with fractures oriented c. N-S, although there is
469 local variability in orientation. Further minor fracture sets are also seen, with significant
470 local heterogeneity in orientation and intensity. Fractures are observed to swing in
471 orientation towards the NE-SW at a mapped bend in the fault. Fracture connectivity and
472 hence bulk permeability is predicted to be higher in the fault bend zone, where fracture sets
473 with different orientations intersect. Fault bends often correspond to local high stress
474 anomalies, and stress rotations resulting in a greater diversity in fracture orientation and an
475 increase in fracture intensity, permeability and fluid flow (e.g. Curewitz and Karson, 1997;
476 Kattenhorn et al., 2000; Tamagawa and Pollard, 2008). The current stress regime in the
477 Bongwana Fault area, is extension oriented approximately NNW-SSE (Brandt, 2011). This
478 suggests that the NE-SW oriented fault bend on the Bongwana Fault at Site B would be in
479 net extension and some rotation of the local stress field would be expected.

480

481 In the detailed fracture intensity maps (Figure 4), shorter length 'small scale' fractures,
482 oriented orthogonal or sub-orthogonal to the c. N-S fractures, are captured. These fractures
483 are missing from in-field measurements at Sites A and C (Figure 3). We suggest this is the
484 result of in-field sampling bias (e.g. Hunter and Donovan, 2005; Bond et al., 2007; Bond,
485 2015) in which the more dominant (longer length and 'thicker') N-S fractures have been
486 preferentially sampled. Although, often 'hairline' in width the increase in fracture
487 connectivity afforded by an orthogonal linking fracture set can drastically increase potential
488 fracture permeability (e.g. Watkins et al., 2015). "Linking" fractures at Site B (the fault bend)
489 show horsetail and splay geometries, and in some outcrops these fractures dominate the
490 fracture population e.g. Site Bii (figure 3c).

491
492 High permeability fracture-dominated pathways controlling spatially distinct CO₂ leakage
493 along a fault in Utah (Burnside et al., 2013). At the Utah site ancient travertine cones record
494 a 400,000+ year history of CO₂ exhalation along the fault, concentrated along high
495 permeability pathways controlled by areas of high fracture density (Dockrill and Shipton,
496 2010), and with a history of sealing and fluid pathway displacement along the fault
497 (Burnside et al., 2013). At Bongwana, there is evidence of fluid-rock interaction, notably at
498 the bend in the fault, where Dwyka Group tillite appears to be altered to kaolinite. So
499 although this fault-bend area is predicted as having a high fracture permeability with
500 respect to the range in fracture orientations, it is possible that this may be reduced or sealed
501 completely due to mineral reactions during CO₂ flux.

502
503 Direct evidence for CO₂ surface exhalations are seen with the presence of travertine cones
504 and gas bubbles effervescing in rivers that cross the mapped fault line. Measurements of
505 ground gas flux and CO₂ concentration across the fracture corridor show a significant flux of
506 CO₂ (191 g m⁻² d⁻¹), with 27% CO₂ measured in the soil gas. The % of CO₂ is significantly
507 above normal back ground levels of <1%. Within c. 50 m of the predicted fault line (on both
508 sides) the CO₂ concentrations and gas flux measurements are consistent with non-elevated
509 levels. Although, we can spatially correlate the CO₂ flux to the fault-line diffusion of the CO₂
510 through the soil will likely obscure any spatial heterogeneity in the flux associated with
511 fractures.

512
513 The CO₂ flux is lower than other cited examples of CO₂ fluxes along fault lines. Gouveia et al.
514 (2005) and Gouveia and Friedmann (2006) measure modern exhalation of CO₂ flux from
515 Crystal Geyser in Utah of 30 tonnes d⁻¹. The flux here however is up a well that was drilled
516 into the fault, giving a point source of CO₂. Values by Roberts et al. (2015) give an average
517 flux of between 10-100 tonnes d⁻¹ for seeps in Italy, although the area over which these
518 values were recorded is not detailed. Annunziatellis et al. (2008) record flux values of CO₂ up
519 faults in the Latera Caldera in Central Italy. The mean CO₂ flux value (1700 g m⁻² d⁻¹) here is
520 very high due to the maximum value of 49563 gm⁻² d⁻¹, while the median value (331 gm⁻² d⁻¹).
521 Data from Beaubien et al. (2008), also from the Latera Caldera, give maximum values of
522 over 90% CO₂ in soil gas and a maximum flux greater than 1600 g m⁻² d⁻¹. Background values
523 were less than 5% and the flux is generally below 10 g m⁻² d⁻¹. Measurements from a
524 traverse near the Laacher See in Germany showed max CO₂ concentrations exceeding 80%
525 and maximum fluxes over 500 g m⁻² d⁻¹. Away from CO₂ vents concentrations were below
526 5% CO₂ with a flux below 50 g m⁻² d⁻¹ (Krueger et al 2011): these data are most comparable
527 to Bongwana. Data from a site near Florina, Greece give max CO₂ concentrations also over

528 80%, with the highest fluxes exceeding $2000 \text{ g m}^{-2} \text{ d}^{-1}$ (max over $9000 \text{ g m}^{-2} \text{ d}^{-1}$). Background
529 values here are similar to those found at Laacher See and Bongwana (Zigou et al., 2013).

530

531 Our favored model for CO_2 flux to the surface at Bongwana is summarized schematically in
532 Figure 8a. We propose that a blind fault is likely genetically linked to the surface through a
533 connected fracture network, exposed on the surface as a fracture corridor, and through
534 which CO_2 and other fluids migrate. In Figure 8b a simplified block diagram illustrates the
535 proposed model for a discrete fault-slip surface and associated fractures at depth connected
536 to the surface through a fracture network. This model differs from the proposed models in
537 Figure 2, which rely on a continuous fault and associated damage zone cropping out at the
538 surface. A theoretical graph of permeability is shown cutting the fracture network (Figure
539 8b). The permeability is determined by the open fracture network permeability. The
540 jaggedness of the permeability graph represents the likely heterogeneities in fracture
541 permeability resulting from the mapped variations in fracture intensity and connectivity
542 mapped, and potential fracture seal due to fluid-rock interaction. Such heterogeneities
543 captured in 2D in the graph would be mirrored along strike resulting in a 3D heterogeneity
544 of CO_2 flux to the surface.

545

546 The true heterogeneity of the fracture network's permeability in controlling CO_2 flow to the
547 surface is untested here. To better understand the genetic link between the fracture
548 network and CO_2 surface exhalation, direct measurements of CO_2 flux on rock outcrops
549 mapped for fractures is proposed as a focus for future work. This provides challenges in
550 ensuring a seal between the rough outcrop surface and the gas capture chamber, but would
551 provide direct evidence of the role of the fracture network permeability in controlling CO_2
552 flux. Given the observation of reaction to kaolinite in the Dwyka Group tillite, in a highly
553 fractured zone, direct measurements of CO_2 flux on fractured outcrop should be combined
554 with detailed petrography to assess the role of fracture seal from fluid-rock interaction.
555 Together such a study could provide not only a present day picture of fracture permeability
556 and CO_2 flux, but a history of flow and fracture seal.

557

558 The connectivity of the Bongwana Fault to the surface through a fracture network has risk
559 implications for fault-bounded CCS sites. For CCS sites that are fault bounded at depth,
560 fractures either associated with the initial faulting or that have formed subsequently due to
561 fault evolution and reactivation may require re-evaluation. Work to better understand the
562 evolution of damage resulting from fault growth and linkage (e.g. Peacock, 2002; Childs et
563 al., 2009; Choi et al., 2016) may inform such evaluations. The observations at Bongwana
564 suggest that rock damage associated with a propagating fault tip (e.g. McGrath and Davison,
565 1995) at depth may create fracture permeability ahead of a discrete slip surface; as seen in
566 hydrothermal systems (Curewitz and Karson, 1997). The bend in the fault, at Site B, could be
567 the result of linkage of two initial fault segments, with the extra fracture damage in this area
568 the result of fracturing ahead of the propagating fault tip prior to linkage. The fracture
569 geometries (horsetails and splays) and orientations are consistent with such a model (Choi
570 et al., 2016). If Site B is a fault linkage zone then we would predict higher fracture
571 permeability at linkage zones, as described by other authors (e.g. Curewitz and Karson,
572 1997; Rotevatn and Bastesen, 2014).

573

574 Fracture networks such as those at Bongwana will not be seismically resolvable, and fault
575 linkage zones may be hard to distinguish in seismic imagery. Interpretation of seismic data
576 of traps for CO₂ storage, may suggest an intact top seal, but could be jeopardized by an un-
577 imaged connected fracture network. Clear understanding of fault geometries and evolution
578 within a regional and local stress field (e.g. Kattenhorn et al., 2000; Healy, 2008) should help
579 to predict fracture deformation patterns. Such studies are crucial to understanding how
580 faults and associated deformation may affect storage integrity for potential fault bounded
581 CCS sites. This understanding is particularly important for fracture networks that are below
582 seismic image resolution.

583

584 **7. Conclusions**

585 Permeability measurements of Dwyka Group tillite suggest that CO₂ stored at depth should
586 be sealed by the tillite. However, field observations of elevated fluid fluxes, and the
587 presence of travertine cones on the surface purport CO₂ flux to the surface. The CO₂
588 exhalations are spatially correlated with a fracture corridor known as the Bongwana Fault.
589 We propose that the CO₂ is exploiting the fracture network to exhale on the surface.
590 Mapped heterogeneity in fracture orientation and intensity suggest that CO₂ flux to the
591 surface will be controlled by localized zones of high permeability along the fracture corridor.
592 Zones of high permeability are created by fracture network connectivity rather than a
593 discrete fault zone. Fracture network connectivity is enhanced by local fault bends that
594 result in fractures with a greater diversity in orientation, as well as local heterogeneity in
595 fracture intensity and connectivity. Further, the spatial distribution of permeability within
596 the fracture network is likely to vary through time as fluid rock interaction seals the
597 fractures.

598

599 The Bongwana Fault, along with other global examples of natural CO₂ seeps, provides
600 evidence that even when there is both a high permeability reservoir and low permeability
601 caprock that localized fracture deformation can result in seal breach. Fractures are often
602 below seismic image resolution, creating an unknown risk in the evaluation of CCS sites.
603 Better understanding of deep-seated fault geometries and deformation around faults,
604 particularly at faults tips and in fault linkage zones, in their regional and local stress field
605 should aid in the prediction of areas of high fracture intensity and hence potential high-risk
606 leakage zones in CCS sites.

607

608 **Acknowledgements**

609 The authors would like to acknowledge the financial support of the UK CCS Research Centre
610 (www.ukccsrc.ac.uk) in carrying out this work. Author Kremer is supported by NERC grant
611 NE/N015908/1. The UKCCSRC is funded by the EPSRC as part of the RCUK Energy
612 Programme. Midland Valley Exploration are thanked for an academic license for Move.
613 Porosity and permeability analysis were undertaken in the University of Aberdeen
614 Petrophysics laboratory with the aid of Sophie Harland. The South African National Energy
615 Development Institute (SANEDI) Stakeholder Engagement team under the South African
616 Centre for Carbon Capture & Storage (SACCCS) is thanked for making the scientific work
617 possible. The National, Provincial and Local Government structures including Traditional
618 Authorities, Municipalities, landowners and local residents are thanked for granting
619 permission to conduct the monitoring in the areas of interest. CGS staff are thanked for

620 their assistance and support in the field. We thank two anonymous reviewers for their
621 comments, which helped to improve the manuscript.

622

623 **References**

624 Agosta, F., and Kirschner, D.L., 2003. Fluid conduits in carbonate-hosted seismogenic normal
625 faults of central Italy. *J. Geophys. Res.* 108, B4. <http://dx.doi.org/10.1029/2002JB002013>.

626

627 Audigane, P., Gaus, I., Czernichowski-Lauriol, I., Pruess, K. and Xu, T., 2007. Two-dimensional
628 reactive transport modeling of CO₂ injection in a saline aquifer at the Sleipner site, North
629 Sea. *American Journal of Science*, 307(7), pp.974-1008.

630

631 Aydin, A. and Eyal, Y., 2002. Anatomy of a normal fault with shale smear: Implications for
632 fault seal. *AAPG bulletin*, 86(8).

633

634 Beaubien, S.E., Ciotoli, G, Coombs, P, Dictor, M. C., Krüger, M, Lombardi, S, Pearce, J.M. and
635 West, J.M. 2008. The impact of a naturally occurring CO₂ gas vent on the shallow ecosystem
636 and soil chemistry of a Mediterranean pasture (Latera, Italy). *International Journal of*
637 *Greenhouse Gas Control*, Vol. 2, 373-387.

638

639 Bense, V.F. and Person, M.A., 2006. Faults as conduit-barrier systems to fluid flow in
640 siliciclastic sedimentary aquifers. *Water Resources Research*, 42(5).

641

642 Bemis, S.P., Micklethwaite, S., Turner, D., James, M.R., Akciz, S., Thiele, S.T., and Bangash,
643 H.A., Ground-based and UAV-based photogrammetry: A multi-scale, high-resolution
644 mapping tool for structural geology and paleoseismology. 2014 *Journal of Structural*
645 *Geology*, v. 69, p. 163–178, doi: 10.1016/j.jsg.2014.10.007

646

647 Bernstein, L., Bosch, P., Canziani, O., Chen, Z., Christ, R., Davidson, O., ... & Kundzewicz, Z.
648 (2007). IPCC, 2007: climate change 2007: synthesis report. Contribution of working groups I.
649 *II and III to the Fourth Assessment Report of the Intergovernmental Panel on Climate*
650 *Change. Intergovernmental Panel on Climate Change, Geneva.* < [http://www.ipcc.](http://www.ipcc.ch/ipccreports/ar4-syr.htm)
651 [ch/ipccreports/ar4-syr.htm](http://www.ipcc.ch/ipccreports/ar4-syr.htm).

652

653 Bond, C. E., Z. K. Shipton, R. R. Jones, R. W. H. Butler, and A. D. Gibbs. 2007. Knowledge
654 transfer in a digital world: Field data acquisition, uncertainty, visualization, and data
655 management. *Geosphere* 3, no. 6 (2007): 568-576.

656

657 Bond, C. E. 2015. Uncertainty in structural interpretation: Lessons to be learnt. *Journal of*
658 *Structural Geology*, 74, 185-200.

659

660 Bond, C.E., Wightman, R. & Ringrose, PS. (2013). 'The influence of fracture anisotropy on CO
661 2 flow'. *Geophysical Research Letters*, vol 40, no. 7, pp. 1284-1289.

662

663 Bretan, P., Yielding, G. and Jones, H., 2003. Using calibrated shale gouge ratio to estimate
664 hydrocarbon column heights. *AAPG bulletin*, 87(3), pp.397-413.

665

666 Burnside, N.M., Shipton, Z.K., Dockrill, B. and Ellam, R.M., 2013. Man-made versus natural

667 CO2 leakage: A 400 ky history of an analogue for engineered geological storage of CO2.
668 *Geology*, 41(4), pp.471-474.

669 Brandt, M. 2011. Seismic Hazard in South Africa Council for Geoscience Report number:
670 2011-0061 © Copyright 2011. Council for Geoscience.

671 Caine, J.S., Evans, J.P. and Forster, C.B., 1996. Fault zone architecture and permeability
672 structure. *Geology*, 24(11), pp.1025-1028.

673
674 Childs, C., Manzocchi, T., Walsh, J.J., Bonson, C.G., Nicol, A. and Schöpfer, M.P., 2009. A
675 geometric model of fault zone and fault rock thickness variations. *Journal of Structural*
676 *Geology*, 31(2), pp.117-127.

677
678 Choi, J.H., Edwards, P., Ko, K. and Kim, Y.S., 2016. Definition and classification of fault
679 damage zones: A review and a new methodological approach. *Earth-Science Reviews*, 152,
680 pp.70-87.

681
682 Curewitz, D. and Karson, J.A., 1997. Structural settings of hydrothermal outflow: Fracture
683 permeability maintained by fault propagation and interaction. *Journal of Volcanology and*
684 *Geothermal Research*, 79(3), pp.149-168.

685
686 De Decker, R.H., 1981. Geology of the Kokstad area. Explan. Sheet 3028. Dep, Miner, Energy
687 Affairs. Pretoria.

688
689 Dingle, R.V. and Scrutton, R.A., 1974. Continental break-up and the development of Post-
690 Paleozoic sedimentary basins around southern Africa. *Bulletin, Geological Society of*
691 *America*, 85, 1467-1474.

692
693 Dockrill, B. and Shipton, Z.K., 2010. Structural controls on leakage from a natural CO 2
694 geologic storage site: Central Utah, USA. *Journal of Structural Geology*, 32(11), pp.1768-
695 1782.

696
697 Duncan, R.A., Hooper, P.R., Rehacek, J., Marsh, J. and Duncan, A.R., 1997. The timing and
698 duration of the Karoo igneous event, southern Gondwana.

699
700 du Toit, A.L., 1946. The geology of parts of Pondoland, East Griqualand. Explanation, Cape
701 Sheet 35, Geological Survey of South Africa.

702
703 Foxford, K.A., Walsh, J.J., Watterson, J., Garden, I.R., Guscott, S.C. and Burley, S.D., 1998.
704 Structure and content of the Moab fault zone, Utah, USA, and its implications for fault seal
705 prediction. *Geological Society, London, Special Publications*, 147(1), pp.87-103.

706
707 Farrell, N.J.C., Healy, D. & Taylor, C.W. (2014). 'Anisotropy of permeability in faulted porous
708 sandstones'. *Journal of Structural Geology*, vol 63, pp. 50-67.

709
710 Faulkner, D., Jackson, C., Lunn, R., Schlische, R. W., Shipton, Z., Wibberley, C., & Withjack, M.
711 O. 2010. A review of recent developments concerning the structure, mechanics and fluid

712 flow properties of fault zones. *Journal of Structural Geology*, 32(11), 1557-1575.
713 [10.1016/j.jsg.2010.06.009](https://doi.org/10.1016/j.jsg.2010.06.009)
714
715 Field, C.B., Barros, V.R., Dokken, D.J., Mach, K.J., Mastrandrea, M.D., Bilir, T.E., Chatterjee,
716 M., Ebi, K.L., Estrada, Y.O., Genova, R.C. and Girma, B., 2014. IPCC, 2014: Climate Change
717 2014: Impacts, Adaptation, and Vulnerability. Part A: Global and Sectoral Aspects.
718 Contribution of Working Group II to the Fifth Assessment Report of the Intergovernmental
719 Panel on Climate Change.
720
721 Fossen, H., Schultz, R.A., Shipton, Z.K. and Mair, K., 2007. Deformation bands in sandstone: a
722 review. *Journal of the Geological Society*, 164(4), pp.755-769.
723
724 Frankel, J.J., 1972. Distribution of Tertiary sediments in Zululand and southern Mozambique,
725 southeast Africa. *American Association of Petroleum Geologists, Bulletin*, 56, 2415-2425.
726
727 Gevers, T.W., 1941. Carbon Dioxide Springs and Exhalations in Northern Pondoland and
728 Alfred County Natal. *Transactions of the Geological Society of South Africa*. 44, 233-301
729
730 Gouveia, F.J., and Friedmann, S.J., 2006, Timing and prediction of CO₂ eruptions
731 from Crystal Geyser, UT: Lawrence Livermore National Laboratory. UCRL-TR, v. 221731, p.
732 16.
733
734 Gouveia, F.J., Johnson, M.R., Leif, R.N., and Friedmann, S.J., 2005, Aerometric
735 measurement and modeling of the mass of CO₂ emissions from Crystal Geyser,
736 Utah: Lawrence Livermore National Laboratory UCRL-TR, v. 211870, p. 59.
737
738 Grab, S. and Knight, J., 2015. Landscapes and landforms of South Africa – an overview. In:
739 Grab, S. and Knight, J. (eds), *Landscapes and landforms of South Africa*. World
740 Geomorphological Landscapes, Springer, Switzerland, 186pp.
741
742 Grunau, H. R. "A WORLDWIDE LOOK AT THE CAP-ROCK PROBLEM." *Journal of Petroleum*
743 *Geology* 10, no. 3 (1987): 245-265.
744
745 Haines, T.J., Michie, E.A.H., Neilson, J.E. & Healy, D. (2016). 'Permeability evolution across
746 carbonate hosted normal fault zones'. *Marine and Petroleum Geology*, vol 72, pp. 62-82.
747
748 Harris, C., Stock, W. D., & Lanham, J. 1997. Stable isotope constraints on the origin of CO₂
749 gas exhalations at Bongwan, Natal. *South African Journal of Geology*, 100(3), 261-266.
750
751 Hartnady, C. J. H. 1985. Uplift, faulting, seismicity, thermal spring and possible incipient
752 volcanic activity in the Lesotho-Natal Region, SE Africa: The Quathlamba Hotspot
753 Hypothesis. *Tectonics*, 4 (4), 371-377.
754
755 Healy, D., 2008. Damage patterns, stress rotations and pore fluid pressures in strike-slip
756 fault zones. *Journal of Geophysical Research: Solid Earth*, 113(B12).
757
758 Hesthammer, J., Johansen, T.E.S. and Watts, L., 2000. Spatial relationships within fault
759 damage zones in sandstone. *Marine and Petroleum Geology*, 17(8), pp.873-893.

760
761 Hunter, A., & Donovan, S. 2005. Field sampling bias, museum collections and completeness
762 of the fossil record. *Lethaia*, 38(4), 305-314.
763
764 Johnson, M.R., Anhaeusser, C.R. and Thomas, R.J. (Eds) 2006. The Geology of South Africa.
765 Geological Society of South Africa, Johannesburg/Council for Geoscience, Pretoria, 691pp
766
767 Johnson, Kendra, Edwin Nissen, Srikanth Saripalli, J. Ramón Arrowsmith, Patrick McGarey,
768 Katherine Scharer, Patrick Williams, and Kimberly Blisniuk. 2014. Rapid mapping of ultrafine
769 fault zone topography with structure from motion." *Geosphere* 10, 969-986.
770
771 Kattenhorn, S.A., Aydin, A. and Pollard, D.D., 2000. Joints at high angles to normal fault
772 strike: an explanation using 3-D numerical models of fault-perturbed stress fields. *Journal of*
773 *Structural Geology*, 22(1), pp.1-23.
774
775 Kim, Y.S. and Sanderson, D.J., 2005. The relationship between displacement and length of
776 faults: a review. *Earth-Science Reviews*, 68(3), pp.317-334.
777
778 King, L.C., 1972. The coastal plain of southern Africa: Its form, deposits and development:
779 *Zeitschr. Geomorphologie*, N.F., Bd. 16, 239-251.
780
781 Kingsley, C.S. and Marshall., C.G.A., 2009. Lithostratigraphy of the Msikaba Formation (Cape
782 Supergroup). South African Committee for Stratigraphy, Lithostratigraphic Series No. 50.
783 Council for Geoscience, 8pp.
784
785 Krüger, M., Jones, D., Frerichs, J., Oppermann, B. I., West, J., Coombs, P., Green, K., Barlow,
786 Y., Lister, R., Shaw, R., Strutt, M. and Möller, I. 2011. Effects of elevated CO₂ concentrations
787 on the vegetation and microbial populations at a terrestrial CO₂ vent at Laacher See,
788 Germany. *International Journal of Greenhouse Gas Control*, Vol. 5, 1093-1098.
789
790 Lake, L.W. (ed). 2007. Petroleum Engineering Handbook, Volumes I-VII. Society of Petroleum
791 Engineers. Accessed via PetroWiki <http://petrowiki.org/PetroWiki>, May 2016.
792
793 Lawther, S.E., Dempster, T.J., Shipton, Z.K. and Boyce, A.J., 2016. Effective crustal
794 permeability controls fault evolution: An integrated structural, mineralogical and isotopic
795 study in granitic gneiss, Monte Rosa, northern Italy. *Tectonophysics*.
796
797 Li, S., M. Dong, Z. Li, S. Huang, H. Qing, and E. Nickel. 2005. Gas breakthrough pressure for
798 hydrocarbon reservoir seal rocks: implications for the security of long-term CO₂ storage in
799 the Weyburn field. *Geofluids* 5, 326-334.
800
801 Li, Z., Dong, M., Li, S., & Huang, S., 2006. CO₂ sequestration in depleted oil and gas
802 reservoirs—caprock characterization and storage capacity. *Energy Conversion and*
803 *Management*, 47(11), 1372-1382.
804
805 Manocchi, T., Walsh, J.J., Nell, P. and Yielding, G., 1999. Fault transmissibility multipliers for
806 flow simulation models. *Petroleum Geoscience*, 5(1), pp.53-63.

807
808 McGrath, A.G. and Davison, I., 1995. Damage zone geometry around fault tips. *Journal of*
809 *Structural Geology*, 17(7), pp.1011-1024.
810
811 Metz, B., Davidson, O., De Coninck, H. C., Loos, M., & Meyer, L. A. (2005). IPCC, 2005: IPCC
812 special report on carbon dioxide capture and storage. Prepared by Working Group III of the
813 Intergovernmental Panel on Climate Change. *Cambridge, United Kingdom and New York, NY,*
814 *USA*, 442.
815
816 Miller, S.A., Collettini, C., Chiaraluce, L., Cocco, M., Barchi, M. and Kaus, B.J., 2004.
817 Aftershocks driven by a high-pressure CO₂ source at depth. *Nature*, 427(6976), pp.724-727.
818
819 Maud, R.R., 1961. A preliminary review of the structure of coastal Natal: Geological Society
820 of South Africa. *Transactions of the Geological Society of South Africa*, 64, 247-256.
821
822 Mauldon, M., Dunne, W.M. and Rohrbaugh, M.B., 2001. Circular scanlines and circular
823 windows: new tools for characterizing the geometry of fracture traces. *Journal of Structural*
824 *Geology*, 23(2), pp.247-258.
825
826 Newell, D.L., Kaszuba, J.P., Viswanathan, H.S., Pawar, R.J. and Carpenter, T., 2008.
827 Significance of carbonate buffers in natural waters reacting with supercritical CO₂:
828 Implications for monitoring, measuring and verification (MMV) of geologic carbon
829 sequestration. *Geophysical Research Letters*, 35(23).
830
831 Otto, J.D.T., 1973. The geology and petrology of the Marble Delta. PhD thesis, University of
832 Stellenbosch. 174pp.
833
834 Partridge, T.C. and Maud, R.R. 2000. Macro-scale geomorphic evolution of southern Africa.
835 In: T.C. Partridge and R.R. Maud (eds), *The Cenozoic of Southern Africa*. Oxford University
836 Press, 3-18.
837
838 Peacock, D.C.P., 2002. Propagation, interaction and linkage in normal fault systems. *Earth-*
839 *Science Reviews*, 58(1), pp.121-142.
840
841 Praetorius, B. and Schumacher, K., 2009. Greenhouse gas mitigation in a carbon constrained
842 world: The role of carbon capture and storage. *Energy Policy*, 37(12), pp.5081-5093.
843
844 Rinaldi, A.P. and Rutqvist, J., 2013. Modeling of deep fracture zone opening and transient
845 ground surface uplift at KB-502 CO₂ injection well, In Salah, Algeria. *International Journal of*
846 *Greenhouse Gas Control*, 12, pp.155-167.
847
848 Ringrose, P.S., Mathieson, A.S., Wright, I.W., Selama, F., Hansen, O., Bissell, R., Saoula, N.
849 and Midgley, J., 2013. The In Salah CO₂ storage project: lessons learned and knowledge
850 transfer. *Energy Procedia*, 37, pp.6226-6236.
851

852 Roberts, J.J., Wood, R.A., Wilkinson, M. and Haszeldine, S., 2015. Surface controls on the
853 characteristics of natural CO₂ seeps: implications for engineered CO₂ stores. *Geofluids*,
854 15(3), pp.453-463.

855

856 Rohrbaugh Jr, M.B., Dunne, W.M. and Mauldon, M., 2002. Estimating fracture trace
857 intensity, density, and mean length using circular scan lines and windows. *AAPG bulletin*,
858 86(12), pp.2089-2104.

859

860 Roncella, R., Forlani, G., & Remondino, F. 2005. Photogrammetry for geological applications:
861 automatic retrieval of discontinuity orientation in rock slopes. In *Electronic Imaging*, p. 17-
862 27. International Society for Optics and Photonics.

863

864 Rotevatn, A. and Bastesen, E., 2014. Fault linkage and damage zone architecture in tight
865 carbonate rocks in the Suez Rift (Egypt): implications for permeability structure along
866 segmented normal faults. *Geological Society, London, Special Publications*, 374(1), pp.79-95.

867

868 Rutqvist, J., 2012. The geomechanics of CO₂ storage in deep sedimentary formations.
869 *Geotechnical and Geological Engineering*, 30(3), pp.525-551.

870

871 Salvini, Riccardo, Silvia Riccucci, Domenico Gulli, Riccardo Giovannini, Claudio Vanneschi,
872 and Mirko Francioni. 2015. "Geological application of UAV photogrammetry and terrestrial
873 laser scanning in marble quarrying (Apuan Alps, Italy)." In *Engineering Geology for Society
874 and Territory-Volume 5*, pp. 979-983. Springer International Publishing

875

876 Schlische, R.W., Young, S.S., Ackermann, R.V. and Gupta, A., 1996. Geometry and scaling
877 relations of a population of very small rift-related normal faults. *Geology*, 24(8), pp.683-686.

878

879 Shipton, Z.K. and Cowie, P.A., 2003. A conceptual model for the origin of fault damage zone
880 structures in high-porosity sandstone. *Journal of Structural Geology*, 25(3), pp.333-344.

881

882 Shipton, Z.K., Evans, J.P., Dockrill, B., Heath, J., Williams, A., Kirchner, D. and Kolesar, P.T.,
883 2006. Natural leaking CO₂-charged systems as analogs for failed geologic storage reservoirs.
884 *Carbon Dioxide Capture for Storage in Deep Geologic Formations—Results from the CO₂
885 Capture Project*, pp.699-712.

886

887 Shukla, R., Ranjith, P., Haque, A., & Choi, X. 2010. A review of studies on CO₂ sequestration
888 and caprock integrity. *Fuel*, 89(10), 2651-2664.

889

890 Sibson, R.H., 1995. Selective fault reactivation during basin inversion: potential for fluid
891 redistribution through fault-valve action. *Geological Society, London, Special Publications*,
892 88(1), pp.3-19.

893

894 Singh, V. and McLachlan, I. 2003. South Africa's east coast frontier offers untested mid- to
895 deepwater potential. *Oil and Gas Journal*, 101(22), 40-45.

896

897 Tamagawa, T. and Pollard, D.D., 2008. Fracture permeability created by perturbed stress
898 fields around active faults in a fractured basement reservoir. *AAPG bulletin*, 92(6), pp.743-

899 764.
900
901 Thomas, R.J., 1988. The geology of the Port Shepstone area. Explanation of sheet 3030
902 (1:250000). Geological Survey of South Africa, 136pp.
903
904 Thomas, R.J., von Brunn, V., Marshall, C.G.A., 1990. A tectono-sedimentary model for the
905 Dwyka Group in southern Natal, South Africa. *South African Journal of Geology*, 93, 809-
906
907 Verdon, J.P., Stork, A.L., Bissell, R.C., Bond, C.E. and Werner, M.J., 2015. Simulation of
908 seismic events induced by CO₂ injection at In Salah, Algeria. *Earth and Planetary Science
909 Letters*, 426, pp.118-129.
910
911 Von Veh, M.W. and Andersen, N.J.B., 1990. Normal-slip faulting in the coastal areas of
912 northern Natal and Zululand, South Africa. *South African Journal of Geology*, 93, 574-582.
913
914 Walker, R.J., Holdsworth, R.E., Imber, J., Faulkner, D.R., Armitage, P.J., 2013. Fault zone
915 architecture and fluid flow in interlayered basaltic volcanoclastic–crystalline sequences. *J.
916 Struct. Geol.* 51, 92–104.
917
918 Walsh, J. J. and Watterson J. 1988. Analysis of the relationship between displacements and
919 dimensions of faults. *J. Struct. Geol.*, 10, 239–247
920
921 Watkeys, M.K. and Sokoutis, D., 1998. Transtension in southeast Africa during Gondwana
922 break-up. In: Holdsworth, R.E., Strachan, R. and Dewey, J.F. (Eds), *Continental
923 Transpressional and Transtensional Tectonics*. Special Publication of the Geological Society
924 of London, 135, 203-214.
925
926 Watkins, H., Bond, C.E., Healy, D., Butler R.W.H., 2015. Appraisal of fracture sampling
927 methods and a new workflow to characterise heterogeneous fracture networks at outcrop.
928 *Journal of Structural Geology*, 72, 67-82.
929
930 Watts, N.L., 1987. Theoretical aspects of cap-rock and fault seals for single-and two-phase
931 hydrocarbon columns. *Marine and Petroleum Geology*, 4(4), pp.274-307.
932
933 Xu, T., Apps, J.A. and Pruess, K., 2003. Reactive geochemical transport simulation to study
934 mineral trapping for CO₂ disposal in deep arenaceous formations. *Journal of Geophysical
935 Research: Solid Earth*, 108(B2).
936
937 Yielding, G., Freeman, B. and Needham, D.T., 1997. Quantitative fault seal prediction. *AAPG
938 bulletin*, 81(6), pp.897-917.
939
940 Young R. B., 1924. Exhalations of Carbon Dioxide in Alfred County, Natal. *Transactions of the
941 Geological Society of South Africa*. 26, 99-102.
942
943 Ziogou, F., Gemeni, V., Koukoulas, N., de Angelis, D., Libertini, S., Beaubien, S.E., Lombardi,
944 S., West, J. M., Jones, D.G., Coombs, P., Barlow, T.S., Gwosdz, S. and Krüger, M. 2013.

945 Potential Environmental Impacts of CO₂ Leakage from the Study of Natural Analogue Sites
946 in Europe. Energy Procedia, Vol. 37, 3521-3528.

947
948

949 **Figure Captions**

950

951 Figure 1. Location map of the field area and sites described. a) Outline of Africa, boxed area
952 defines the location of map b. b) Outline of South Africa, grey box outlines map c. c)
953 Geological map of the KwaZulu-Natal and Eastern Cape area of South Africa around Port
954 Edward, after Gevers (1941), based on the mapping of du Toit (1920). d) Enlargement of the
955 boxed area in c. showing the localities of the sites visited, and the local occurrence of CO₂
956 seeps.

957

958 Figure 2. Hypothetical models for permeability across fault zones. a) The fault core/slip-
959 surface (red -line) is permeable and acts as a conduit for fluid. b) The fault core and the
960 surrounding damage zone are permeable and act as a conduit for fluid. c) The fault core
961 and/or slip surface is impermeable, but the surrounding damage zone is permeable and act
962 as a conduit for fluid. d) permeability distribution is heterogeneous across the fault core
963 and/or slip surface and the surrounding damage zone.

964

965 Figure 3. Structural data from the three field sites, shown in their spatial context with
966 respect to the Bongwana Fault and CO₂ seeps. a) Geological map of the field area based on
967 Gevers (1941) after the mapping of du Toit (1920), showing the spatial distribution of the
968 three field sites, annotated with stereonet of measured fractures. b) Google Map satellite
969 image showing the locations of images for Site B (figure part c) and Site C (figure part d), the
970 fault trend mapped by du Toit and Gevers (1941) is shown by the white dashed line. Note
971 the significant change in fault orientation between the sites. Stereonets show the mean
972 fault-fracture orientation at Site Cii and Site Biv, and slickenside trend and plunge
973 measurements (N=3 and N=14 respectively). c) Google Map satellite image of Site B,
974 showing sub-sites i-iv and the associated fracture measurements at each sub-site. An
975 approximate fault trend is shown by a dashed white line, star denotes site of CO₂ bubbles in
976 the river. d) Google Map satellite image of Site C, showing sub-sites i-ii and the associated
977 fracture measurements at each sub-site. Long dashed white line is the approximate fault
978 trend, smaller dashed white lines outline travertine mounds around the Umtavuna River
979 CO₂ exhalations. Present day CO₂ seeps are marked by white stars; the black star denotes
980 the site of a now extinct CO₂ travertine cone. e) 3D photogrammetric image of the main
981 active travertine cone, the cone is approximately 1.5m wide. All stereonet plots are equal
982 area lower hemisphere projections (poles to fracture planes); rose plots, for the same
983 fractures, are at 5 degree intervals.

984

985 Figure 4. Interpretations of fractures in orthorectified photographs created from virtual
986 outcrop models. Each figure part shows the fracture interpretation and associated rose
987 diagrams of fracture orientations, and a contour map of fracture density for each site. The
988 sites are shown in figure 2 and are a) Site A, Fractures N=446; east fractures N=211, west
989 fractures N=235; b) Site Bi, Fractures N=142; c) Site Biii, Fractures N=103; d) Site Ci,
990 Fractures N=2285 and e) Site Cii, Fractures N=31.

991 Figure 5. Analysis of the effect of circle radius on fracture trace network parameters. a)
 992 Graph of fracture density, intensity and mean trace length against radius size. b) Location of
 993 circle centres used in the analysis on fracture trace map for site Ci.

994 Figure 6. The measured CO₂ ground flux at Site C. a) The aerial photograph shows the
 995 location of the nearby CO₂ seeps (white stars active travertine cones, black star non-active
 996 travertine cone). Coloured circles are measurement points scaled for gas flux and CO₂
 997 concentration % in the soil. b) Actual measurements are shown in the inset graph.
 998

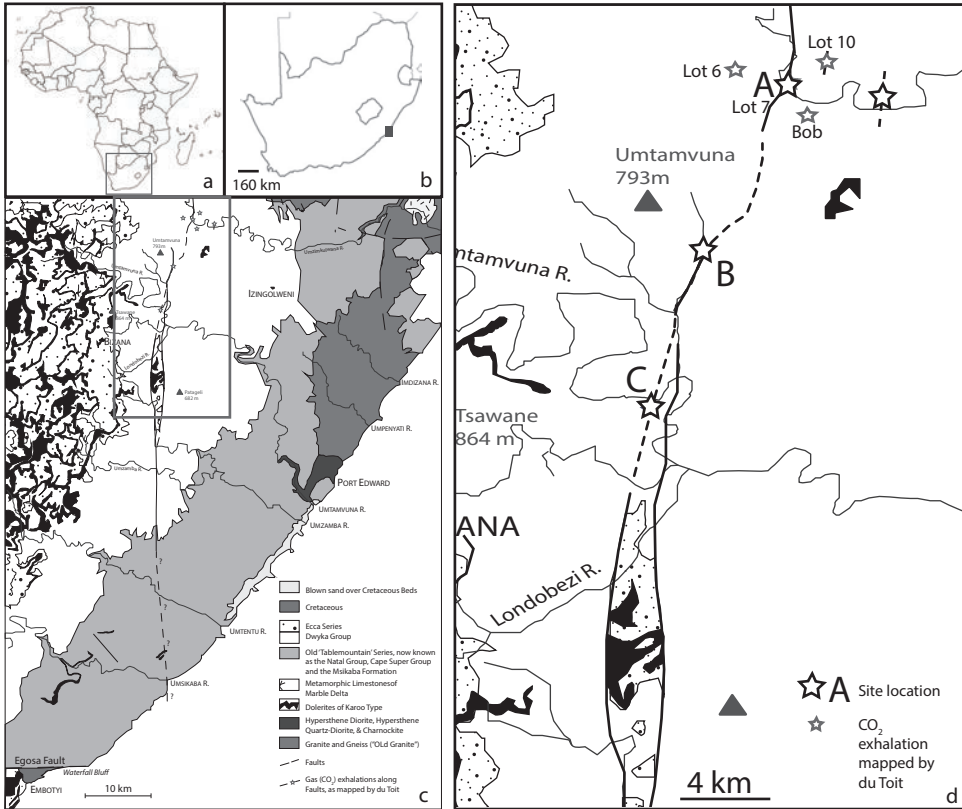
999 Figure 7. Porosity – log Permeability plot of sandstones. The plot shows the porosity-
 1000 permeability ranges of sandstones from unconsolidated sands to tight sandstone, based on
 1001 the Society of Petroleum Engineers, Petrowiki . The porosity and permeability values of the
 1002 Msikaba Formation sandstone and Dwyka Group tillite are annotated.
 1003

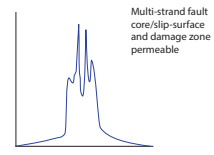
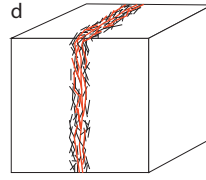
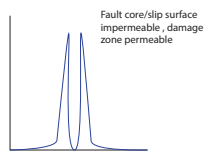
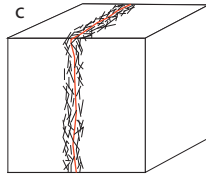
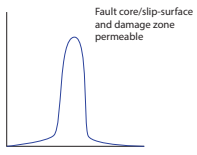
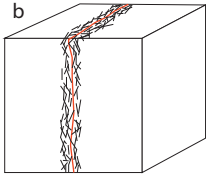
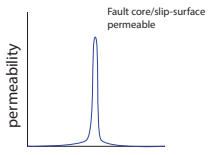
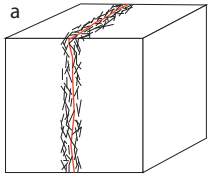
1004 Figure 8. Summary model for CO₂ flow to the surface at the Bongwana Fault. a) Proposed
 1005 model for a deep-seated fault connected to the surface via a fracture corridor. Complexities
 1006 in fault geometry at depth, bends and asperities, create zones of more distributed damage
 1007 observed in the fractures at the surface. This creates a more connected fracture network
 1008 and a higher fracture permeability due to a greater range in fracture orientation. b)
 1009 Simplified block model of a fault at depth (thin red line) with connection to the surface via a
 1010 high permeability fracture network (black lines). The theoretical permeability graph, shows
 1011 a potential range in permeability created by complexities in the fracture network that may
 1012 control the leakage pathway for CO₂ to the surface.
 1013

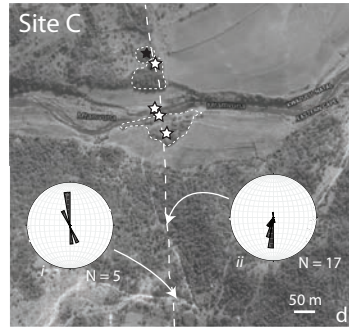
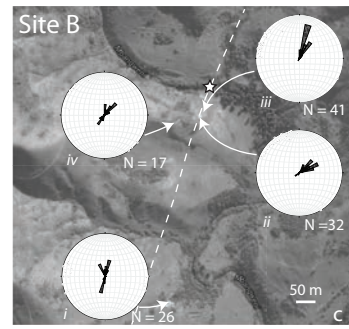
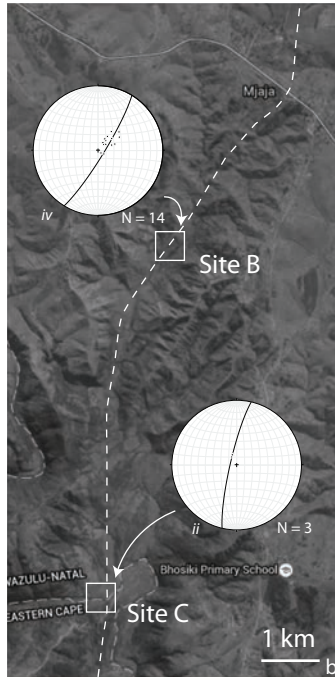
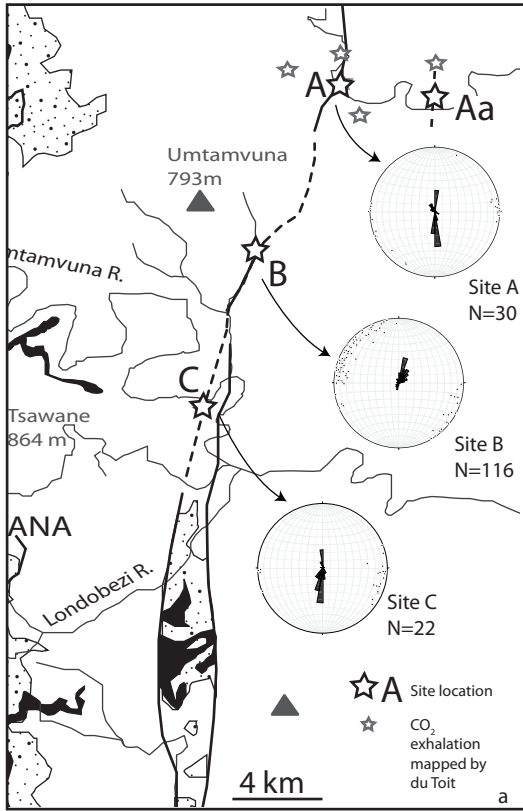
1014 **Table**

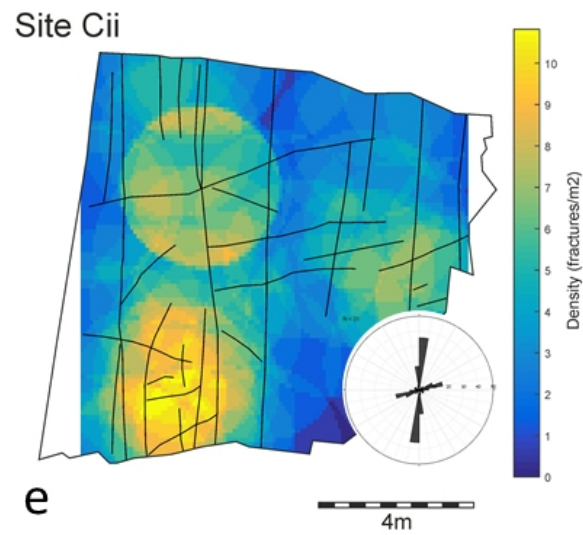
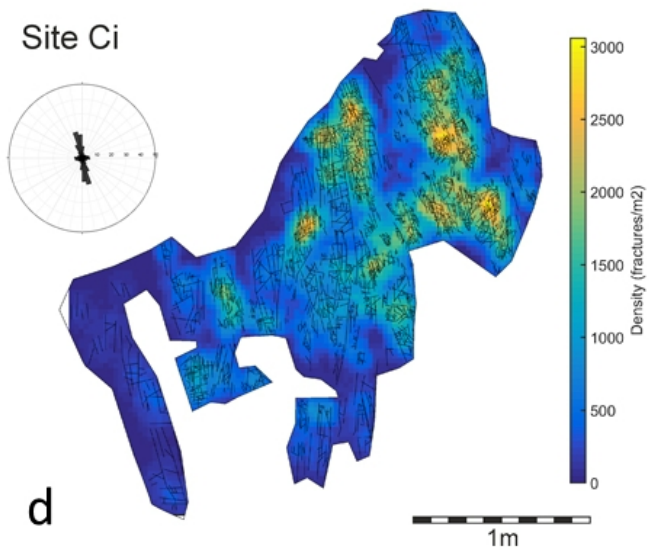
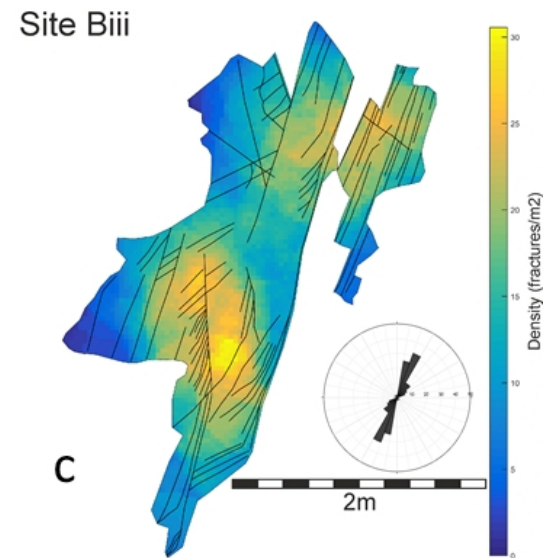
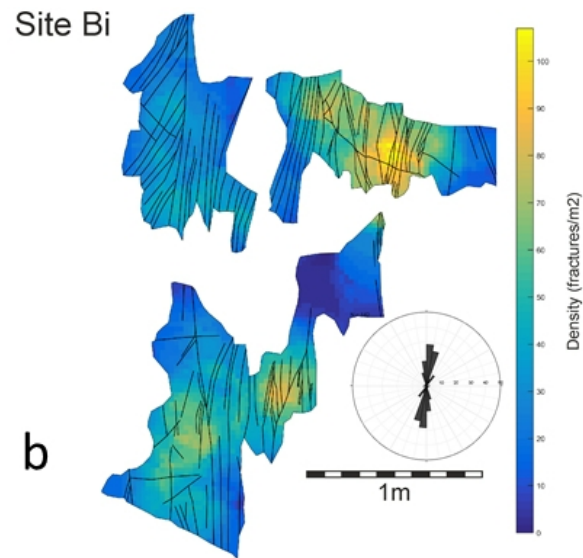
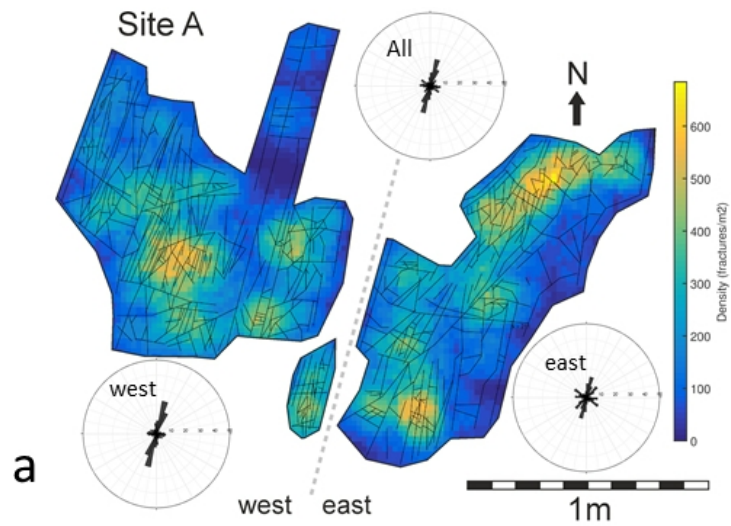
Sample	Porosity ϕ (He) %	Permeability - KL (N ₂)(mD)
<i>Msikaba Formation sandstone</i>		
20V -orthogonal to bedding	4.1	0.1865
20P - parallel to bedding	4.7	0.2762
20O - parallel to bedding orthogonal to 20P	4.4	0.2587
<i>Dwyka Group tillite</i>		
14V -vertical	22.8	0.0709
14O - orthogonal	21.2	0.0629

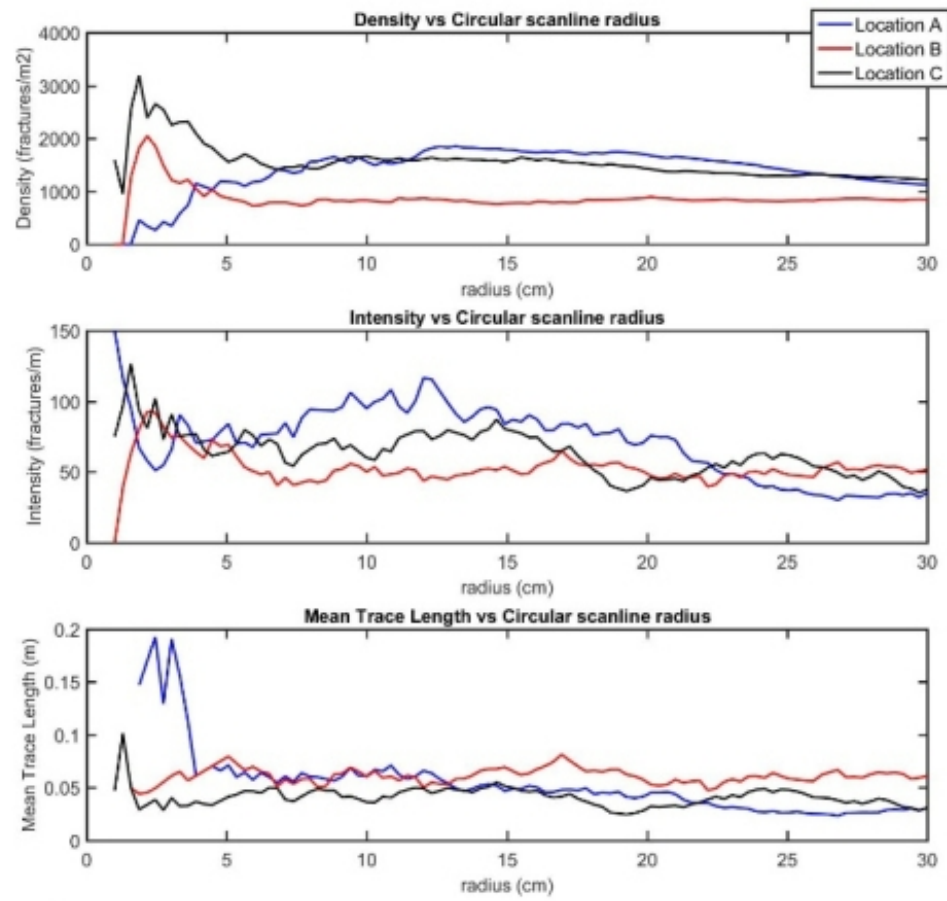
1016
 1017 Table 1. Porosity and permeability measurements of the Msikaba Formation sandstone and Dwyka Group
 1018 tillite.
 1019



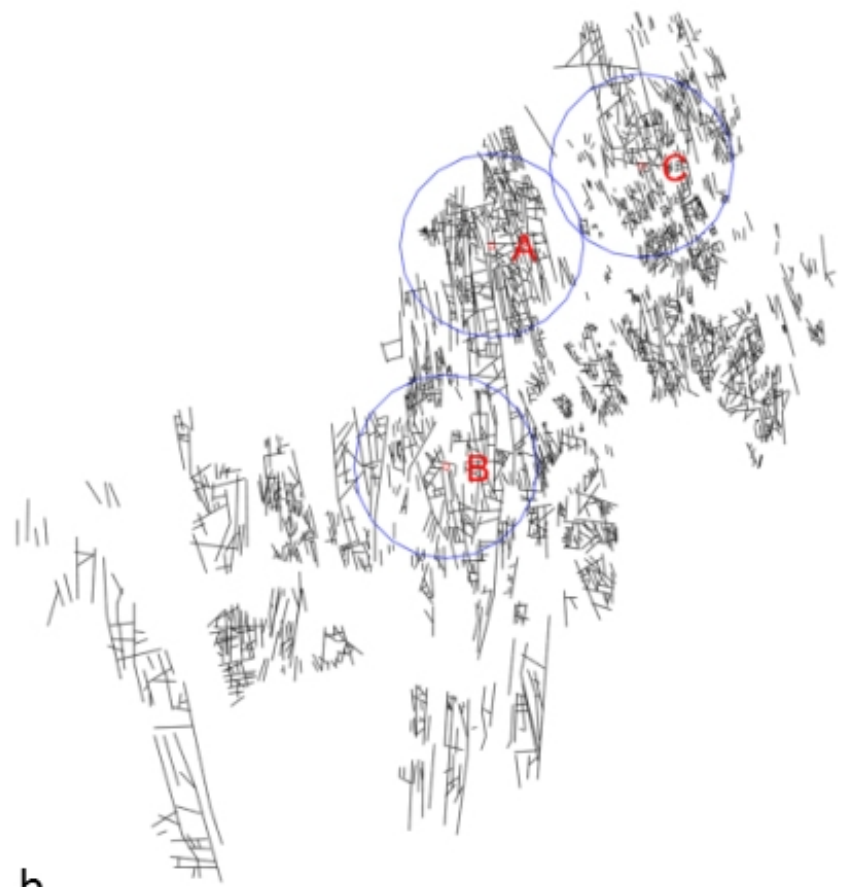




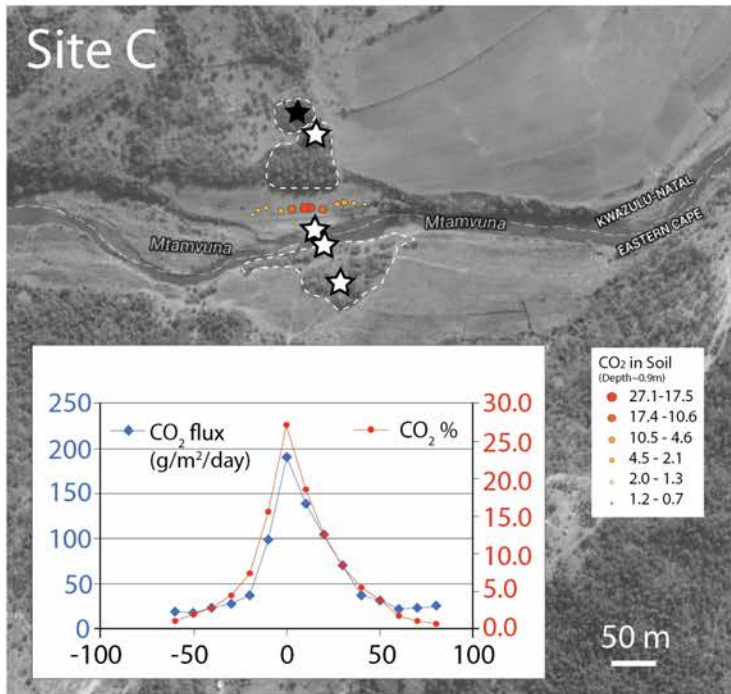


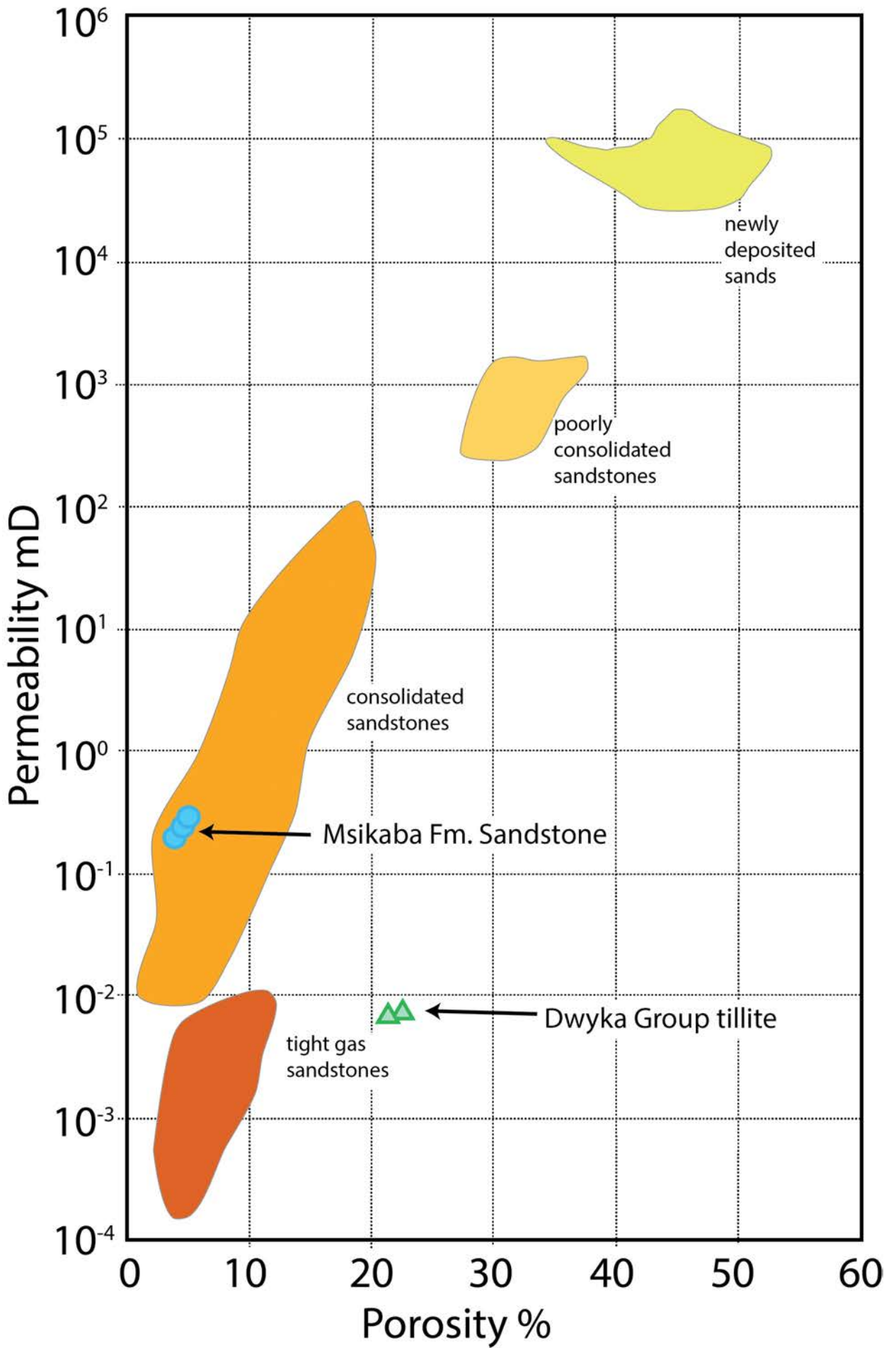


a

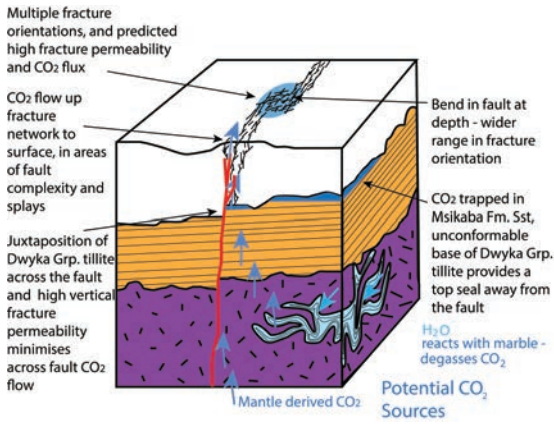


b

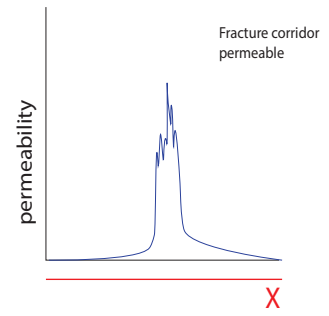
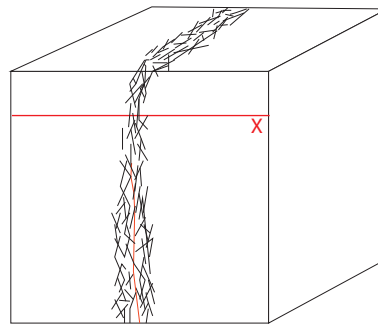




a



b



Highlights

- CO₂ migration is spatially associated with the Bongwana fault fracture corridor.
- Cap rock permeability suggests that without fractures it would act as a flow barrier.
- Elevated CO₂ concentration and flux are measured across the fracture corridor.
- Fracture intensity and orientation variability creates permeability heterogeneity.
- Seismically unresolvable fracture networks may impact CO₂ storage capability.